Mixing A-type and G-type B-site antiferromagnetism in AMn_{1-x}Fe_{x}O_{3}(A=La,Nd)

D. M. Pajerowski

Phys. Rev. B **98**, 134431 — Published 17 October 2018

DOI: 10.1103/PhysRevB.98.134431

Mixing A-type and G-type, *B*-site Antiferromagnetism in AMn$_{1-x}$Fe$_x$O$_3$ (A = La, Nd)

D. M. Pajerowski[1]

[1]Neutron Scattering Division, Oak Ridge National Laboratory, Oak Ridge, TN 37831, USA

Abstract. Using a classical Heisenberg model with anisotropic nearest neighbor superexchange and uniaxial anisotropy, I investigate the magnetic order of the transition metals on the *B*-sites in AMn$_{1-x}$Fe$_x$O$_3$ (A = La, Nd; x = [0,1]) with Monte Carlo methods. Magnetic parameters are extracted from pre-existing experimental data when available and otherwise estimated with calculations. Superexchange energies are compared to density functional theory and anisotropy energies to ligand field theory, and the potential for doping induced strain affecting these parameters is considered. I find co-existence regions of different types of magnetic order (A-type and G-type antiferromagnetism), regions with distinct magnetic transitions for the two order parameters, non-collinear ground states for intermediate values of x that decrease the amplitude of the ordered moment in a way consistent with experiment for low dopings, and a reproduction of the experimentally determined non-monotonic interpolation of the ordering temperatures. The detailed shape of the phase boundaries in (x,T)-space is found to be diagnostic of the magnetic interactions. These results also suggest a ferrimagnetic ground state for the A_2MnFeO$_6$ double perovskite with a $T_N \approx 270$ K for A = La and Nd.

I. Introduction

The magnetic phase diagrams of doping and ordering for GdFeO$_3$-type [1] orthometallates with mixed manganese and iron on the pseudo-perovskite *B*-site and a light rare earth on the *A*-site have some features that are not well explained. The specific unknowns in those materials that sparked this study are: the dependence of the ordering temperature upon doping, the existence of multiple phase transitions (often dubbed spin re-orientations) for mixings near the 50% level, the determination of the moment direction and magnitude, the possibility of doping induced stresses to modify the magnetic parameters, and the nature of the interaction between manganese and iron sites. The aspects that dictate these magnetic phenomena are interconnected and interrogated here with some calculations.

This type of doping and mixing of magnetic centers is a common theme across many materials as a method to tune desirable properties and explore nature. Intermediate mixings may have emergent phenomenon that are not simply linear combinations of the end-members due to interactions (and competition) between the pure constituents. Consider the mixing of an A-type antiferromagnet with a G-type antiferromagnet. A famous example of this mixing is the La$_{1-x}$Ca$_x$MnO$_3$ (LCMO) series that substitutes on the *A*-site of the *AB*O$_3$, orthomanganite lattice to vary between A-type $La^{3+}Mn^{3+}O^{2-}{}_3$ (LMO) and G-type $Ca^{2+}Mn^{4+}O^{2-}{}_3$ (CMO). The LCMO is an important series because it is a host of fundamental physics, as the Mn^{3+}/Mn^{4+} double exchange, and applied physics, as the colossal magnetoresistance (CMR); other divalent and trivalent *A*-site substitutions can produce similar results. [2] A less studied series $La^{3+}Mn_{1-x}{}^{3+}Fe_x{}^{3+}O^{2-}{}_3$ (LMFO)

is generated by doping on the *B*-site, between LMO and the G-type antiferromagnet $LaFeO_3$ (LFO), whereby the additional constituent interactions are Fe^{3+}/Mn^{3+} superexchange (J_{MnFe}). The LMFO and the $NdMn_{1-x}Fe_xO_3$ (NMFO) that is between $NdMnO_3$ (NMO) and $NdFeO_3$ (NFO) will be the main topic of this investigation, and specifically the phase diagram of the *B*-site magnetism. So, *B*-site magnetic order in (x,T)-space of the $AMn_{1-x}Fe_xO_3$ (AMFO) series is focused on here.

The desire to understand AMFO magnetism is bolstered by recent reports on chemically ordered films. Examples of double perovskite manganese-iron films include La_2MnFeO_6, [3,4] the putative multiferroic Bi_2MnFeO_6, [5–10] and magnetic property calculations on the as yet un-synthesized Ho_2MnFeO_6. [11] Without chemical order, $(La_{0.5}Bi_{0.5})(Mn_{0.5}Fe_{0.5})O_{3.9}$ films have been reported as multiferroic. [12] Anyway, especially for ion pairs with close ionic radii, chemical order is rarely perfect in double perovskites and understanding the solid solution phase is a coupled problem. Moreover, an open question is whether double exchange physics can exist between Fe^{3+}/Mn^{3+} sites in LMFO. [13]

The magnetism of NMFO and LMFO is similar, as they are light rare earths that are close on the periodic table of elements. While there are various papers on LMFO, one must be careful when assigning conclusions to observations as a parasitic third dimension of this series is along the Mn^{4+} direction due to oxidation during firing. [14] LMFO is attractive to consider as a starting point for *B*-site magnetic properties because the *A*-site has a closed shell, but there is more experimental data available in the low-Mn^{4+} regime for NMFO. Indeed, the crystal structures of NMFO and LMFO are similar, both orthorhombic *Pnma* (alternatively *Pbnm*), [15,16] and the main difference is more distortion of the oxygen bridges in NMFO owing to the smaller ionic radius and larger electronegativity of Nd compared to La. [17]

The magnetic phase diagrams of NMFO and LMFO motivates this study. The interpolation of magnetic ordering temperatures between the orthoferrite and orthomanganite endmembers is non-monotonic for NMFO [15,18,19] and LMFO (for low concentrations of Mn^{4+} as in LMO, [20] $LaMn_{0.8}Fe_{0.2}O_3$, and LFO [20]), Figure 1. Overall, the dependence of onset ordering upon the iron fraction, x, is similar for NMFO and LMFO, aside from a decrease in transition temperatures for Nd-based compounds. A first insight into the minimum in the ordering temperature with doping can come from assuming the magnetic modes to be completely orthogonal, where the magnetic order parameter in the mean field approximation would only depend upon the number of nearest neighbors (NNs) having the same magnetic point symmetry. [21] Additional details of percolation and order parameter interaction require a non-averaging theory and knowledge of J_{MnFe}, which will be part of this work. For $NdMn_{0.5}Fe_{0.5}O_3$, Figure 1 shows two magnetic transitions, and the cause of the second transition is not quantified. Various reports on the detailed magnetic structures of AMFO compounds have been performed, but detailed models of mode amplitudes for the different magnetic symmetries are lacking. For example, neutron diffraction of NMFO observes mode contributions that are less than a weighted average of the end-members. [18,22,23] Secondary to these experimental observations is the

need to understand the magnetic superexchange J_{MnFe} that is expected to exist between Mn^{3+} and Fe^{3+} in these systems, and to understand how incorporating ions into non-native lattices can affect the magnetics of those ions and of the host lattice.

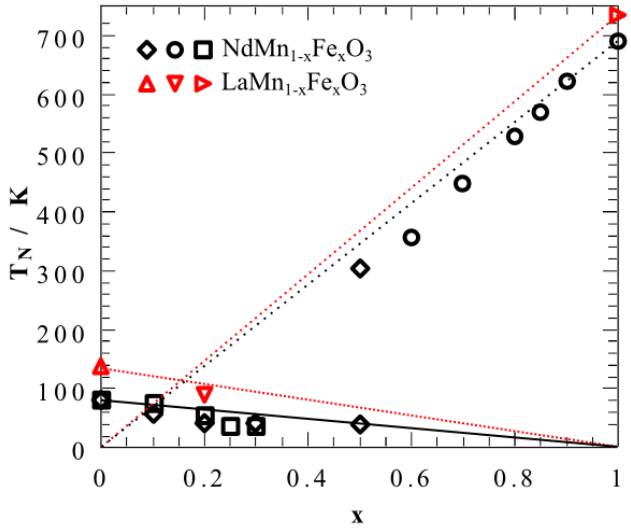

Figure 1: Experimental Néel temperatures of $NdMn_{1-x}Fe_xO_3$ (◇, [18] ○, [15] □ [19]) and $LaMn_{1-x}Fe_xO_3$ (△, [14] ▽,[manuscript under review in PRB] ▷ [20]). There is a non-monotonic dependence of the Néel temperature, T_N, on the iron doping, x. Lines are a scaling of end-member ordering temperatures by the number of end-member nearest neighbors.

Following this introduction, section II presents the computational frameworks used. Section III reviews end-member properties and extends the experimentally available magnetic parameters with calculations, while considering the potential effects of doping induced strain. Section IV contains the Monte Carlo calculations of the phase diagram, based upon the parameter set results of Section III. A discussion of the results that considers the doping dependence of magnetic order is in section V and summarizing conclusions are in section IV.

II. Computational Methods

A. Hamiltonian parameters

The fewest number of energies that might reproduce the phase diagram in Figure 1 are considered here. Antisymmetric exchange is important for orthometallates, specifically in determination of weak ferromagnetism, but is a higher order effect for the transition temperature determination as is the magnetic dipolar interaction. For NMFO, the *A*-site can affect the magnetic order, but at temperatures less than 10 percent of the onset of magnetic order, and so

the Nd moments are not used here. Next nearest neighbor (NNNs) superexchange is necessary to explain the magnetism in heavier rare-earth orthometallates with atomic numbers greater than 62, [24] setting a limit to this model's applicability.

The Hamiltonian considered has single-ion anisotropy and NN interactions. The single-ion Hamiltonian local anisotropy depends on if a site is occupied by Mn or Fe. The local anisotropy direction is not along a crystallographic direction, but rather it is dictated by the local axes. For the metal ion numbering scheme in Figure 2 (a) of *Pnma*, the directions are $D_{M1} = (x,y,z)$, $D_{M2} = (x,y,-z)$, $D_{M3} = (x,-y,z)$, $D_{M4} = (x,-y,-z)$. While the *Pnma* is the standard setting and is used here, the *Pbnm* setting is popular for orthometallates and both have been used historically. The average anisotropy axis is along a crystallographic axis due to the symmetry constraints of the space group. The NN superexchange interactions may be different in the basal ac-plane versus the b-axis, and each site experiences a local superexchange field that depends on its neighbors. Here, ferromagnetic (FM) alignment is for $J > 0$ and antiferromagnetic (AFM) or ferrimagnetic alignment is for $J < 0$. These superexchange energies are shown pictorially in the context of the crystalline lattice in Figure 2 (b-e).

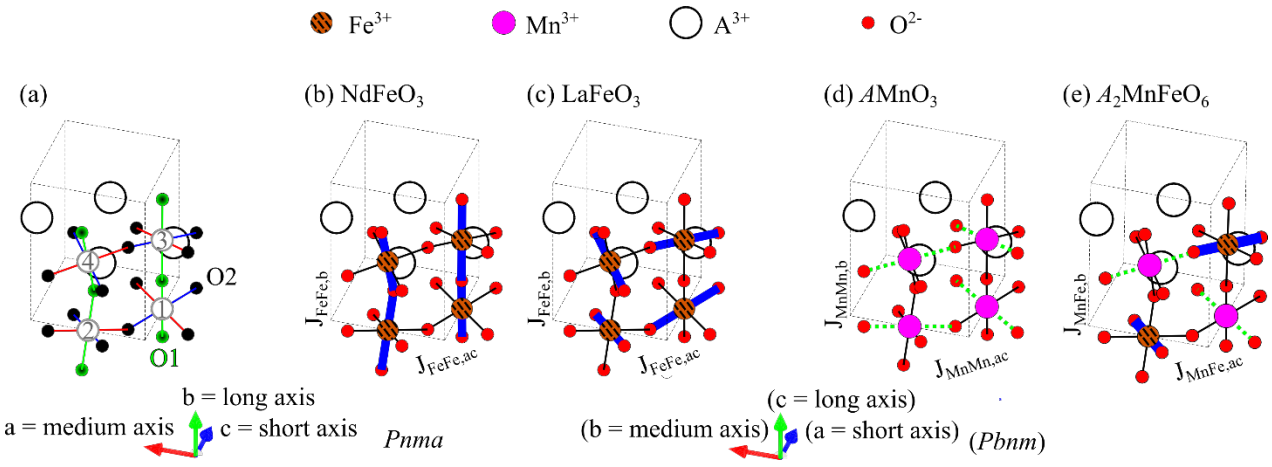

Figure 2: Crystal structures. (a) The *Pnma* (*Pbnm*) structure of AMFO has one Wyckoff position for the transition metal that is replicated 4 times in the unit cell and there are two distinct oxygen positions. (b) $NdFeO_3$ orthoferrite structure. (c) $LaFeO_3$ orthoferrite structure. (d) Orthomanganite structure. (e) Double perovskite structure. For the images in (b) to (e), Fe-O short bonds are thick blue lines, and Mn-O long bonds are dotted green lines.

B. Density Functional Theory

Density functional theory (DFT) as applied here requires one to choose functionals, pseudo-potentials, and on-site Coulomb interaction that agree with observables. For $LaMeO_3$ (where Me

= Cr, Mn, Fe, Co, or Ni) experimental electronic band gap energies and magnetic moment amplitudes could be reasonably reproduced in the local spin density approximation (LSDA) with anisotropic Coulomb interactions U and J. [25] The orthomanganites are more sensitive than orthoferrites to DFT parameterization, as there is feedback between the structure and magnetic ground-state via the Jahn-Teller distortion, and FM and A-type AFM ground states are close in energy. [26] Here, the best fit parameters from the DFT exploration of LMO are used; U_{Mn} = 8.0 eV and J_{Mn} = 1.9 eV. [27] These parameters were then scaled by the U_{Fe}/U_{Mn} ratios found to best fit for LSDA+U|J LMO and LFO [25] to give U_{Fe} = 8.7 eV and J_{Fe} = 2.1 eV. The VASP software [28,29] was used with the generalized gradient approximation (GGA) functional of Perdew-Burke-Erzenhof as PBE. [30] The projector augmented wave (PAW) method [31,32] was used for valence electrons with the included pseudo-potentials applied via the PBE.54 files: La (11, [Kr4d]), Nd_3 (11, [Xe4]), Fe_sv (16, d7s1), Mn_sv (15, 3p4s3d), and O (6, s2p4) where valence electrons, states are in parentheses. A Γ-centered mesh was generated with (5 × 4 × 5) k-points, and plane waves were cut above a kinetic energy of 520 eV. Relaxed structures used experimental structures as the initial conditions for LMO, NMO, LFO, and NFO, and the average of the LMO and LFO structures for La_2MnFeO_6 and the average of the NMO and NFO structures for Nd_2MnFeO_6.

Superexchange parameters can be estimated from DFT by considering energies of different spin configurations. Here, four different spin configurations are considered: (F) ferromagnetism, A-type AFM, C-type AFM, and G-type AFM. See Figure 3 (a-c) for illustration. These superexchange energies are

$$J_{ij,b}[GC] = \frac{E_G - E_C}{(2\text{ bonds} \times 4\text{ atoms})S_iS_j} \quad (1)$$

$$J_{ij,ac}[GA] = \frac{E_G - E_A}{(4\text{ bonds} \times 4\text{ atoms})S_iS_j} \quad (2)$$

$$J_{ij,b}[AF] = \frac{E_A - E_F}{(2\text{ bonds} \times 4\text{ atoms})S_iS_j} \quad (3)$$

$$J_{ij,ac}[CF] = \frac{E_C - E_F}{(4\text{ bonds} \times 4\text{ atoms})S_iS_j} \quad (4)$$

where i = Mn or Fe and j = Mn or Fe. From this, there are two values for J_b (using GC or AF) and J_{ac} (using GA and CF), so the lowest energy states are used to extract superexchange such that for an A-type AFM $J_b \equiv J_b[AF]$ and $J_{ac} \equiv J_{ac}[GA]$.

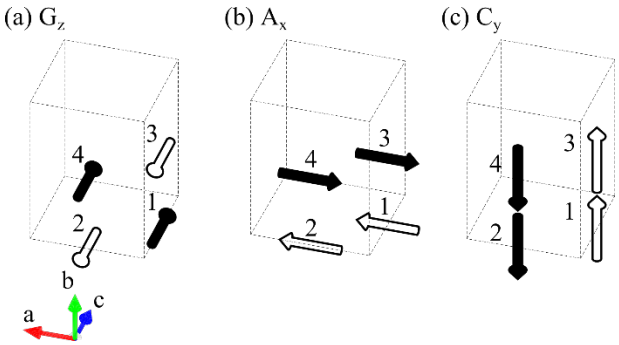

Figure 3: Magnetic structures. Three different magnetic modes are shown, including the (a) z orientation of the G-type magnetism of LFO and NFO, (b) the x orientation of the A-type magnetism of LMO and NMO, and (c) the y orientation of C-type magnetism. Arrow coloration is associated with spin direction.

C. Monte Carlo

Monte Carlo (MC) methods have been used extensively in the simulation of magnetic systems. Here, I consider a classical Heisenberg model in a MC methodology with a slightly different practical implementation.

To begin, there are two local variables associated with each site, the angle of azimuth, ϕ, and the angle of elevation, θ, as measured with respect to the crystallographic (z) c-axis. There is a local parameter with a probability weighted by the doping fraction that keeps track of the type of atom at the local sites, which selects single-site anisotropy energy and NN superexchange interactions. At the beginning of a simulation, angular variables corresponding to moment orientation are randomized. The ordered indexation of the sites is then copied with a random order, which is used during update processes to avoid artifacts from ordered updates.

When a site is selected during a thermalization update, the local fields are calculated to give the energy surface. The minimum energy direction is calculated numerically, and a new coordinate system of ϕ' and θ' is defined for that unique axis z'. To reduce the energy calculation calls, the value of ϕ' is chosen with a flat random probability, then θ' is discretized into n_θ different angles, from which a weighted probability obeying Boltzmann statistics is chosen. A rotation back to the crystallographic ϕ and θ is performed before moving to the next site. This update process is first repeated for a number of burn-in steps (n_{burn}) until the energy is stabilized, and then repeated (n_{update}) until sufficient data on the thermalized state exist for calculation of magnetic properties. Matrix numerics are performed using NumPy objects [33] with LAPACK [34] diagonalization routines, and MINPACK [35] minimization routine, implemented via SciPy. [36] A discussion of finite size effects is in Appendix A.

D. Single-ion magnetic properties

The single-ion physics of Mn^{3+} and Fe^{3+} is considered in the context of ligand field theory (LFT) with the AOMX program, [37] to explore structure induced anisotropy changes. The angular overlap Hamiltonian has electron-electron interactions that utilize Racah parameters $B = \beta_B B_0$ and $C = \beta_C C_0$, ligand field interactions that are written in the angular overlap formalism to have e_s and e_p that scale with distance as r^{-n}, and a spin orbit interaction parameterized by $\zeta = k\zeta_0$. [38] This leaves six parameters (β_B, β_C, e_s, e_p, n, k) that must be determined in order to calculate the single-ion anisotropy, which is extracted from the spin-orbit splitting of the ground term. A discussion of the single-ion parametrization scheme is in Appendix B.

III. End-members, double perovskites, and foundations for solid solution calculations

A. Experimental magnetic parameters

Literature on the un-doped end-members of AMFO is presented in preparation for comparison to simulations. The available magnetic structures, NN superexchange energies, and single-ion anisotropies are recounted.

Using the language of symmetries, the magnetic order of the undoped compounds can be described. In the *Pnma* structural space group of AMFO, there are four magnetic irreducible representations for the *B*-site: Γ_1, Γ_3, Γ_5, and Γ_7. [39] These tabulations may be written in a notation that describes the magnetic symmetry with a letter and a subscript corresponding to the moment direction, [40] such that $\Gamma_1 = (G_x, C_y, A_z)$, $\Gamma_3 = (C_x, G_y, F_z)$, $\Gamma_5 = (A_x, F_y, G_z)$, and $\Gamma_7 = (F_x, A_y, C_z)$, corresponding to magnetic space groups *Pnma*, *Pn'm'a*, *Pn'ma'*, and *Pnm'a'*, respectively. If in the non-standard *Pbnm* setting, $\Gamma_1 = (A_x, G_y, C_z)$, $\Gamma_3 = (F_x, C_y, G_z)$, $\Gamma_5 = (G_x, A_y, F_z)$, and $\Gamma_7 = (C_x, F_y, A_z)$, corresponding to magnetic space groups *Pbnm*, *Pbn'm'*, *Pb'n'm*, and *Pb'nm'*, respectively. A way to try to avoid confusion of the unique crystal axis setting is to write these irreducible representations as $\Gamma_1 = (A_S, G_M, C_L)$, $\Gamma_3 = (F_S, C_M, G_L)$, $\Gamma_5 = (G_S, A_M, F_L)$, and $\Gamma_7 = (C_S, F_M, A_L)$, where the subscripts denote the short (S), medium (M), and long (L) crystallographic axes; although, materials have been refined with different short and medium axes symmetries even while the primary directions of the manganite local Jahn-Teller distortions are in both cases along the medium axis. [14]

These orthomanganites order as A-type antiferromagnets, and weak FM is present due to magnetocrystalline anisotropy and antisymmetric exchange. [41] Neutron diffraction gives Γ_5 for the *B*-site magnetism, and an ordered moment of $A_x = 3.87\ \mu_B$ ($T_N = 140$ K) for LMO [42], $A_x = 3.80\ \mu_B$ ($T_N = 82$ K) for NMO (reported as A_y within *Pbnm*), [43] and other modes less than the detection limit of the experiment. The LMO neutron scattering experiments included oriented-crystal-inelastic work that extracted $J_{MnMn,b} = -0.58$ meV, $J_{MnMn,ac} = 0.83$ meV, and $D_{Mn} = -0.165$ meV while powder inelastic in a different series of experiments extracted $J_{MnMn,b} = -1.1$ meV, $J_{MnMn,ac} = 1.85$ meV, and $D_{Mn} = -0.6$ meV. [44]

These orthoferrites order as G-type antiferromagnets, also having weak FM due to antisymmetric exchange. [45] While the original work on LFO showed G-type AFM with an ordered moment of G_z (reported as G_x for *Pbnm*) = 4.6 μ_B (T_N = 750 K), [20] later high resolution measurements needed an additional mode to fit the magnetic structure at room temperature. [46] There are structural changes as a function of temperature present in LFO, [47] which are linked to magnetic reorientations in orthoferrites, [45,48] but no spin rotation in LFO has been explicitly reported. In NFO, these reorientations have been measured to take place between 90 K and 120 K, and after an onset of ordering with G_z (reported as G_x for *Pbnm*), G_y (reported as G_z for *Pbnm*) components become dominant in the low temperature limit where a range of values for the ordered moment of NFO are reported to be between 4.2 μ_B and 4.5 μ_B (T_N = 670). [49] Light scattering of NFO give $J_{FeFe,b}$=$J_{FeFe,ac}$=-5.4 meV and a maximum value of D_{Fe}=0.02 meV, where the anisotropy has a temperature dependence. [48,50] Powder inelastic neutron scattering on LFO give $J_{FeFe,b}$=$J_{FeFe,ac}$=-4.87 meV and D_{Fe} less than the resolution of the measurement. [44] Single crystal inelastic neutron scattering was fit with a Hamiltonian containing antisymmetric exchange and NNN superexchange to give $J_{FeFe,b}$=$J_{FeFe,ac}$=-5.50 meV, $D_{Fe,z}$ = -0.0179 meV (reported as $D_{Fe,x}$ for Pbnm), $D_{Fe,y}$ = -0.0145 meV (reported as $D_{Fe,z}$ for Pbnm). [51]

So, there is a good foundation to understand the magnetism of the NMFO and LMFO end-members. Unfortunately, there is not yet spectroscopic evidence to determine the J_{MnFe} interaction that will be present in solid solutions, although one potential experimental anchor point is from strained La_2MnFeO_6 films that showed a transition temperature of 230 K. [4] Often, attempts are made to apply Goodenough-Kanamori rules [52,53] to at least determine the sign of the J_{MnFe} interaction, but there is a chance for error with anisotropic ions having bond angles different than 180°. Therefore, the approach here is to check DFT against experiment for $LaFeO_3$, $LaMnO_3$, $NdFeO_3$, and $NdMnO_3$, and then extend to the double perovskites of La_2MnFeO_6 and Nd_2MnFeO_6 to guide choosing $J_{MnFe,b}$ and $J_{MnFe,ac}$ values for solid solutions.

B. Calculations of magnetic parameters (with strain considered)

Magnetic parameters are calculated with DFT and LFT. Density functional theory is used to calculate geometries and NN superexchange of LFO, NFO, LMO, NMO, La_2MnFeO_6, and Nd_2MnFeO_6. Zero field splittings can be computed for the different local structures, from DFT and experiment. For discussions of strain, a new parameter ξ is introduced that is the iron fraction of the structural lattice considered (not the iron fraction of the ions). For LMFO, the DFT lattice constants may then be expressed in units of Å as a = 5.566+0.014ξ, b = 5.925–0.280ξ, c = 7.692+0.225ξ, and V = 253.651–4.273ξ, and for NMFO a = 5.464+0.212ξ, b = 5.972–0.305ξ, c = 7.587+0.255ξ, and V = 247.613–3.979ξ. The local environments of the short (s), medium (m), and long (l) metal to oxygen bonds units of Å are then s = 1.925+0.107ξ, m = 1.984+0.051ξ, and l = 2.270–0.228ξ for LMFO and s = 1.925+0.105ξ, m = 1.975+0.056ξ, and l = 2.283–0.177ξ for NMFO. Or, in terms of Jahn-Teller modes (Q_2 = 2(l–s)/$\sqrt{2}$ and Q_3 = 2(2m–l–s)/$\sqrt{6}$), Q_2(LMFO) = 0.488–0.474ξ, Q_3(LMFO) = –0.185–0.182ξ, Q_2(NMFO) = 0.506–0.399ξ,

and Q_3(NMFO) = –0.211–0.150ξ. The metal-oxygen-metal NN bond-angles may be expressed as ∠LMFO = 151.361+2.303ξ and ∠NMFO = 148.024+2.087ξ. Tabulations and additional descriptions of the LFT and DFT results are available in Supplemental Material, [54] which also shows the deviations from structure interpolation of end-members for the double-perovskites and additional comparisons to experimental data. [55–59]

The effect of strain induced by transition metal substitution on the superexchange in LMFO and NMFO was investigated by performing electronic relaxations in non-ionically-relaxed structures, e.g. LFO electronic energies calculated in the LMO structure that is not the ground state structure of LFO and retains net-ionic forces. These strain results are shown with ground state results in Figure 4. For $LaFeO_3$ and $NdFeO_3$, the transfer to Jahn-Teller distorted structures of $LaMnO_3$ and $NdMnO_3$ has the effect to increase the magnitude of $J_{FeFe,ac}$ and decrease the magnitude of $J_{FeFe,b}$ while retaining the G-type AFM. There is an approximate linear dependence of the DFT iron-iron interaction upon the iron fraction of the structural lattice, ξ, whereby for $NdFeO_3$ $J_{FeFe,b}$/meV = –3.99 – 0.98(1-ξ) and $J_{FeFe,ac}$/meV = –4.42 + 0.58(1-ξ), and for $LaFeO_3$ $J_{FeFe,b}$/meV = –4.11 – 0.87(1-ξ) and $J_{FeFe,ac}$/meV = –4.57 + 0.63(1-ξ). For $LaMnO_3$ and $NdMnO_3$, the effect of transferring to the less distorted structures (towards $LaFeO_3$ and $NdFeO_3$) is a change in the ground state from A-type AFM to a FM half-metal with greatly increased superexchange interactions. The DFT manganese-manganese interactions as a function of ξ are approximately quadratic, such that for $NdMnO_3$ $J_{MnMn,b}$/meV = –0.27 + 5.50ξ² and $J_{MnMn,ac}$/meV = +0.05 + 5.69ξ², and for $LaMnO_3$ $J_{MnMn,b}$/meV = –0.26 + 7.93ξ² and $J_{MnMn,ac}$/meV = +0.27 + 7.36ξ². For La_2MnFeO_6 and Nd_2MnFeO_6, the G-type (ferrimagnetic) ground state is robust when straining towards the more or less distorted parent phases.

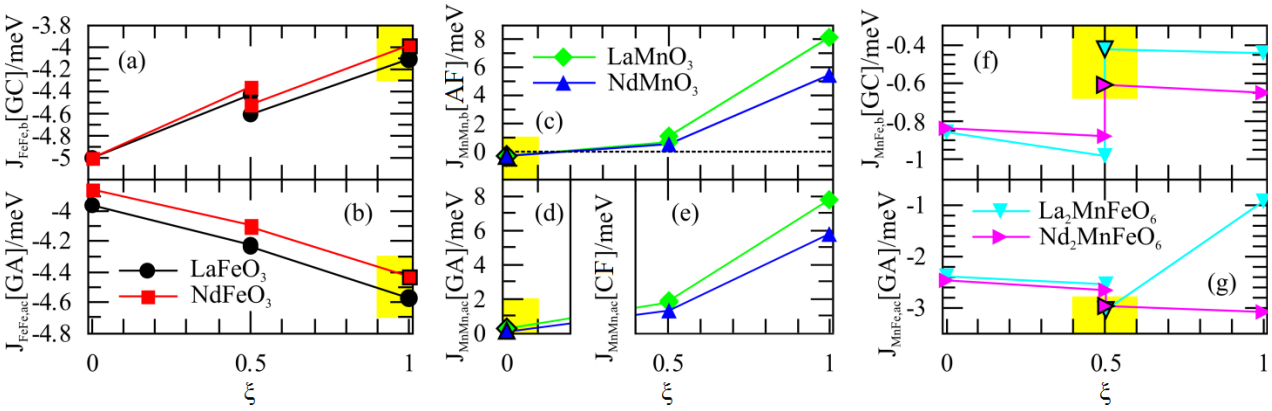

Figure 4: Density functional theory obtained exchange constants in non-relaxed structures. The ground states have symbols surrounded by a black outline with a highlighting yellow box, and the lines connect from left to right to a manganite structure (ξ = 0), to an average of manganite and ferrite structure (ξ = 0.5), to the double perovskite structure (ξ = 0.5), to the ferrite structure (ξ = 1). The structural lattice doping values, ξ, are for the structures and the ions in the calculations are denoted in the figure legends.

Doping induced strain may influence the magnetic anisotropy. This LFT model directly connects the first coordination sphere with the magnetic anisotropy, Figure 2. The trend of the local structure effect on the single-ion anisotropy magnitude is visualized as a function of the iron fraction of the host lattice structure, ξ, in Figure 5. An approximately linear dependence of magnitude is found for both ions. For Mn^{3+}:LMFO, $|D_{Mn}| = 0.16+0.06\xi$ and for Mn^{3+}:NMFO, $|D_{Mn}| = 0.16+0.09\xi$. For Fe^{3+}:LMFO, $|D_{Fe}| = 0.002+0.050(1-\xi)$ and for Fe^{3+}:NMFO, $|D_{Fe}| = 0.005+0.049(1-\xi)$. The local distortions take $|D_{Fe}|$ from being a few percent of $|D_{Mn}|$ at $\xi = 1$ to the same order of magnitude as $|D_{Mn}|$ for $\xi = 0$ (the Jahn-Teller distorted structure).

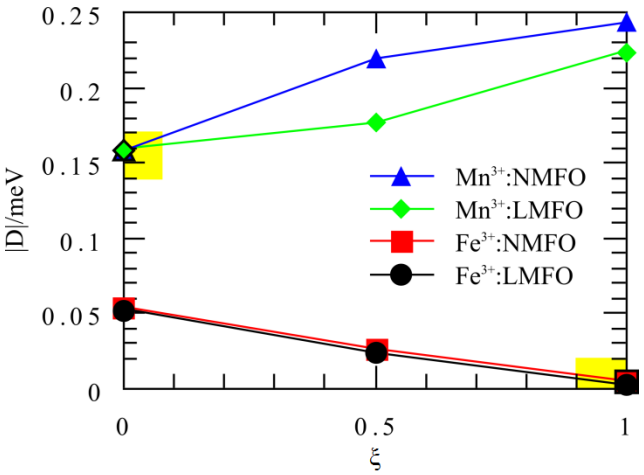

Figure 5: Single-ion anisotropy magnitudes in different environments. Using the local environments from DFT, the Mn^{3+} and Fe^{3+} anisotropies in different local environments are shown. The horizontal axis variable ξ tracks the structure in which the ion is considered, and the ions are connected to symbols in the legend. The $\xi = 0.5$ is the double perovskite structure, and the local environment specific to the ion is used. The native states have symbols surrounded by a black outline with a highlighting yellow box.

Monte Carlo simulations are used to model magnetic phase transitions of the chemically ordered systems, based upon the NN superexchange and single-ion anisotropy. The magnetic ordering temperature in the absence of single-ion anisotropy should be directly proportional to the superexchange energy in this classical MC model as $T_{N,CMC} = 1.494\ JS^2$ (Appendix A) and for this anisotropic case it is estimated as $T_{N,CMC} = 1.494 \frac{(|J_b|+2|J_{ac}|)}{3} S_i S_j$. The experimental ordering temperatures are listed in Table I. For the orthoferrites, experiments have not reported any anisotropy between the superexchange in the basal plane and along the pseudo-tetragonal crystal axis, and here the ratio for the two values is taken from the DFT result and the overall

magnitude fit to the observed Néel temperature. The DFT values had to be scaled by 1.54 and 1.49 times to reproduce the observed T_N via MC for LFO and NFO, respectively. Therefore, the DFT values for the double perovskites were also scaled by 1.5 times, which gave transition temperatures of 270 K and 265 K for La_2MnFeO_6 and Nd_2MnFeO_6, respectively. The value for La_2MnFeO_6 is close to the 230 K reported for a film, [4] although the interpretation here is ferrimagnetic while it is presumed FM in the film. For $LaMnO_3$, the ratio of interplane and intraplane coupling is taken directly from the spin wave experiment and magnitude is fit to the observed T_N. For $NdMnO_3$, it was seen in the DFT that the $J_{MnMn,b}$ is robust with respect to lanthanide substitution, so the ordering temperature was fit to a varying $J_{MnMn,ac}$ with $J_{MnMn,b}$ taken directly from the $LaMnO_3$ fit. Using the scaling law for $T_{N,CMC}$ would give 1.31 meV for $NdMnO_3$ $J_{MnMn,ac}$, but from a series of MC runs it was found that 0.95 meV reproduces the experimental ordering temperature and this difference is attributed to the highly anisotropic superexchange parameters in that compound. The derived superexchange parameters are summarized in Table II.

Table I: Experimental ordering temperatures of end-member compounds.

	$LaMnO_3$ [14]	$NdMnO_3$ [43]	$LaFeO_3$ [20]	$NdFeO_3$ [60]
T_N/K	138	82	738	689

Table II: Monte Carlo superexchange parameters estimated from consideration of experiment, DFT, and MC in concert. As described in the text, the exchange parameters were scaled to match the simulated and (where available) experimental ordering temperatures.

	La	Nd
$J_{FeFe,b}$/meV	-6.34	-5.93
$J_{FeFe,ac}$/meV	-7.05	-6.57
$J_{MnFe,b}$/meV	-0.66	-0.87
$J_{MnFe,ac}$/meV	-4.35	-4.16
$J_{MnMn,b}$/meV	-1.55	-1.55
$J_{MnMn,ac}$/meV	2.12	0.95

IV. AMFO Monte Carlo simulations

Using the results from Section III, MC simulations of AMFO solid solutions may be performed. The J_{MnFe} interaction is not experimentally available, and tests were performed to check the signs of $J_{MnFe,ac}$ and $J_{MnFe,b}$. Fixing the magnitudes due to approximate agreement with the ordering temperature in double perovskite films, the J_{MnFe} signs are changed such that the double perovskite would give A-type AFM, FM, C-type AFM, or G-type AFM, where the G-type AFM double perovskite would have a net ferrimagnetic moment.

The ordering temperatures extracted from the models, by fitting the sub-lattice moments below T_N to be proportional to $(T\text{-}T_N)^{-\beta}$, are shown in Figure 6 (a) and (b). The critical exponent β was fixed to the three dimensional cubic Heisenberg model value of 0.366. [61] The model of $J_{MnFe} = 0$ shows good agreement with the experimental ordering temperatures for most dopings, although a suppressed transition with respect to the experimental data available (for $NdMn_{1-x}Fe_xO_3$) begins to emerge in the vicinity of x = 0.5. If the double perovskite A_2MnFeO_6 were to have A-type AFM order, the parameters in Table II may be used except for setting $J_{MnFe,ac} = |J_{MnFe,ac}|$ to be FM in the ac-plane. The small iron doping regime shows a qualitative disagreement with the experimental data, whereby the J_{MnFe} = A-type model has an initial increase in T_N rather than the experimentally observed initial decrease. If A_2MnFeO_6 would be FM, the parameters in Table II may be used except for $J_{MnFe,b} = |J_{MnFe,b}|$ and $J_{MnFe,ac} = |J_{MnFe,ac}|$, which gives FM interactions for all directions. This model does reproduce the initial decrease in T_N with x for low values of the iron doping, x, but tends to overshoot for intermediate dopings. If A_2MnFeO_6 were to have C-type AFM order, the parameters in Table II may be used except for $J_{MnFe,b} = |J_{MnFe,b}|$ that gives FM lines of spins along the b-axis. This C-type model also tends to initially increase T_N for small values of x, as did the A-type model, contrary to experiment. If A_2MnFeO_6 were to have an arrangement of G-type AFM order, as in a ferrimagnetic order, all of the parameters in Table II may be used. This G-type model has the best agreement with the experimental data.

The mixing of different magnetic orders may give rise to non-collinear spin arrangements, which is seen in the spin-direction-pair-correlation-function (spin collinearity) that is the spin-pair-correlation-function without inclusion of the magnitude and only direction, Figure 6 (c) and (d). This spin collinearity may be expressed as $\sum_{NN} \frac{|S_i \cdot S_j|}{|S_i||S_j|}$. For $J_{MnFe} = 0$, the spin collinearity is decreased with doping due to the different easy directions of Mn and Fe in the system. For the $J_{MnFe} \neq 0$ models there is a competition between the Fe-dominated order and the Mn-dominated order to give well defined minima as a function of doping. There is a tendency for energy to minimize by having order parameters of different symmetry to point along orthogonal crystal axes. The position of the minima is dependent on the model parameters.

The dominant types of magnetic symmetries observed are A-type and G-type and J_{MnFe} influences the mixed region. These phases may be visualized by considering the sublattice magnetization, which is shown as a function of doping for the $J_{MnFe} = 0$, J_{MnFe} = G-type, and J_{MnFe} = A-type models in Figure 6 (e-j). The larger anisotropy of Mn dominates the easy axis consideration, while for Fe the anisotropy is small enough that this simulation does not rigorously lock those moments in a given direction. Without any interaction between the manganese and iron, the per site moments are retained up to a percolation limit and stick to the parent symmetries. When interactions between manganese and iron are introduced, the majority magnetic order tends to induce a degree of that majority order onto the minority ions, and vice versa. In specific terms, for x = 0.2 $NdMn_{0.8}Fe_{0.2}O_3$ with J_{MnFe} = G-type as in Figure 6 (g), the

majority magnetic order is A-type and the minority magnetic order is G-type, where most of the Mn is A-type but there is a finite G-type Mn component and most of the Fe is G-type but there is a finite A-type Fe component. The cross-over from A-type to G-type majority magnetic order depends upon the J_{MnFe} interaction, Figure 6 (g-j)

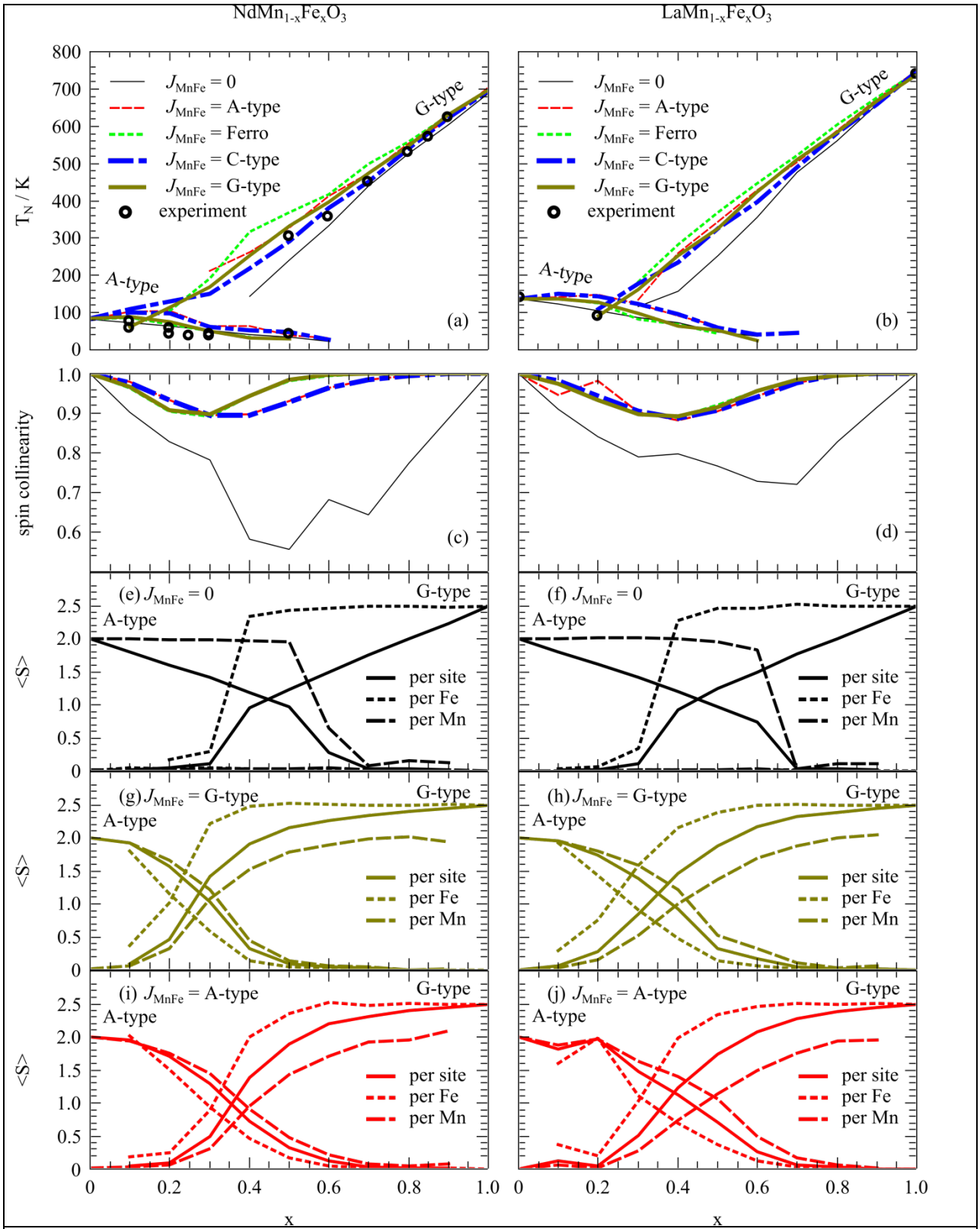

Figure 6: Monte Carlo simulations with different symmetries of J_{MnFe} interaction. Experimental data points defining the magnetic phase diagram, as in Figure 1, are compared to the different models in (a) and (b). Using the same legend as the phase diagram, the spin collinearity at 1 K is

shown in (c) and (d). The magnitude of the A-type and G-type ordered moments in terms of the spin moment, <S>, are shown with a normalization to the total number of sites, the manganese contribution per manganese, and the iron contribution per iron in (e-j).

For a given symmetry of k = (0,0,0) magnetic order (i.e. ferro, A-type, C-type, G-type), there will be a preferred direction as in Figure 3. Consider the J_{MnFe} = G-type series that was found to be most consistent with calculations and experiment. Taking the direction of D_{Mn} to be along a unique axis *u*, the MC derived A-type and G-type order parameters may be further broken down to components parallel and perpendicular to *u*. Invisible in Figure 6, there is a doping induced spin re-orientation between x = 0.2 and x = 0.3 from ($A_{\parallel u}$, $G_{\perp u}$) to ($G_{\parallel u}$, $A_{\perp u}$), where the ambiguity of the direction perpendicular to *u* may be resolved by a rhombic anisotropy. Taking *u* to be along the medium crystallographic axis (M) that corresponds to the long Mn-O bond for $NdMnO_3$, the doping induced phase transition as x increases from 0.2 to 0.3 can be written as going from (A_M, $G_{\perp M}$) to (G_M, $A_{\perp M}$) or in terms of what irreducible representations allow those moments, Γ_5 = (G_S, A_M, F_L) to Γ_1 = (A_S, G_M, C_L). In the absence of experimentally determined information about the local coordination spheres of the ions with doping, these MC simulations used the end-member parameters supplemented with the double perovskite parameters for J_{MnFe}. There is then a large parameter space of doping dependent superexchange and anisotropy that is deemed too large to explore without additional observables. For example, consider the $NdMn_{0.5}Fe_{0.5}O_3$ calculation. For the end-member parameters, this gives the (G_M, $A_{\perp M}$) order as dictated by $D_{Mn}||M \gg D_{Fe}$. However, if D_{Fe} becomes increased due to strain, MC simulations show an eventual stabilization of a ground state satisfying D_{Fe}. For example, if $D_{Fe}||S$ and D_{Fe} is similar to D_{Mn}, then a (G_S, $A_{\perp S}$) order is seen, or if $D_{Fe}||L$ and D_{Fe} is similar to D_{Mn}, then a (G_L, $A_{\perp L}$) order is seen. The result that persists is that the competing types of order align to orthogonal axes.

V. Discussion

An investigation of the magnetism in $AMn_{1-x}Fe_xO_3$ (*A* = La, Nd) has been presented. Considering the known experimental parameters for nearest neighbor (NN) superexchange and uniaxial anisotropy, and then furthering with density functional theory (DFT) and angular overlap based ligand field theory (LFT), a classical anisotropic Heisenberg Monte Carlo (MC) simulation was performed. This study has ignored antisymmetric exchange, NNN superexchange, and the rare-earth magnetism. The DFT and LFT parameters are semi-quantitative for the end-members, with some scaling applied before simulation to reproduce the experimental ordering temperatures. The main MC simulation was done with end-member parameters and is a frame of reference for extension to strained parameter MC simulations.

The nature of the J_{MnFe} interaction between manganese and iron sites is modelled in double perovskites. A G-type ground state for both Nd_2MnFeO_6 and La_2MnFeO_6 is found in DFT, with a slight strain dependence (Figure 4 (f)) that does not de-stabilize the ground state symmetry and suggests G-type arrangement will persist in strained films. This ferrimagnetic ground state is in

disagreement with the FM ground state postulated for La_2MnFeO_6, [4] but does agree with the observation of a net moment in that material. A similar G-type ground state was found in a DFT study of Ho_2MnFeO_6. [11] The AFM J_{MnFe} interaction also has the best agreement with the experimental dependence of T_N upon x (Figure 6 (a)).

The dependence of the ordering temperature on doping in $AMn_{1-x}Fe_xO_3$ is reproduced. A semi-qualitative agreement is found for all symmetries of interspecies interaction (J_{MnFe}) considered, but quantitative aspects of the phase diagram change for different models tried. The non-monotonicity of T_N upon x is a generic property of compounds having incompatible order parameters. The ground state of these orthomanganites being A-type and these orthoferrites being G-type, in the intermixed regions the system cannot accommodate both types of order simultaneously for a given spatial coordinate and there is a competition. In general, a third type of order may emerge from interactions between the parent phases, but in this case the interaction between the parent phases is the same symmetry as the orthoferrite end-member.

The experimental observation of two phase transitions for $NdMn_{0.5}Fe_{0.5}O_3$ [18,23] can be explained by a co-existence of symmetrically distinct end-member-type superexchange-driven order parameters. From the model here, the first transition ($T_{N,1} \approx 250$ - 300 K) is then a Fe-G-type dominated transition and the second transition ($T_{N,2} \approx 50$ K) may be assigned to an Mn-A-type dominated transition. This Mn order parameter for the second phase transition at $T_{N,2}$ is physically distinct from other posited order parameters: neodymium induced [23] as has been inferred from the $T_{Nd} \approx 20$ K transition in $NdMnO_3$ [42] and the octahedral rotation induced spin-reorientation native to $NdFeO_3$ between 90 K and 120 K. [49]

There are model phase transitions that are not experimentally observed in magnetic neutron diffraction. The extension of these MC results to long-range order in a real material is ambiguous because of the finite simulation size. For L = 22 as for AMFO simulations, taking the metal to metal distances of ≈4 Å, this corresponds to an 8.8 nanometer domain. In $LaMnO_3$, domain sizes are closer to 30 nanometers. [62] Therefore, a short-range order giving rise to clusters of spins that is not spatially phase-coherent even in a single domain may be expected for the extreme doping values where a minority magnetic order is seen.

The superexchange interactions may be modified by doping induced stresses. This response of superexchange to stress was analyzed by tracking the DFT energies while forcing lattices to adopt strained structures, e.g. considering the magnetism of LFO ions on a fixed LMO lattice structure. While J_{FeFe} and J_{MnFe} both change with the structure, the G-type symmetry of the superexchange interaction is robust. On the other hand $J_{MnMn,b}$ changes sign for some strained geometries considered, even as $J_{MnMn,ac}$ does not, changing from A-type interactions to FM. This sensitivity of J_{MnMn} is expected to cause magnetic disorder in doped systems.

The magnetic anisotropies may be modified by doping induced stresses, and a model was developed that connects the first coordination sphere of the transition metals to the single-ion

anisotropies. The effect of structure on the S = 2 trivalent manganese ion magnetic anisotropy is well represented in the literature due to connection with Jahn-Teller effects, while the S = 5/2 trivalent iron ion is less so. Taking s, m, and l to refer to the short, medium, and long metal to oxygen bond lengths, the LFT model here showed that Fe-O(s) and Mn-O(l) dictate the easy directions for D_{Fe} and D_{Mn} (respectively). [54] Connecting to the crystallographic lattice (where S, M, and L to refer to the short, medium, and long crystallographic axes), this shows how D_{Mn} || M and D_{Fe} || L or M, with dipolar anisotropy having a similar magnitude as D_{Fe} for AFeO$_3$. The analysis of local anisotropy for A_2MnFeO$_6$ showed that D_{Fe} || L and D_{Mn} || M for the double perovskite, Figure 2 (e). Consider then the influence of strain. The data in Figure 6 use the native anisotropies, where the uniaxial anisotropy D_{Mn} in AMnO$_3$ is two orders of magnitude larger than D_{Fe} in AFeO$_3$, and while experimental determination of local ion octahedra is lacking, the double perovskite calculations of $\xi = 0.5$ in Figure 5 have D_{Mn} only ≈6 times larger than D_{Fe}. These results show that the direction and magnitude of D_{Fe} will be modified from the AFeO$_3$ values for appreciable manganese doping of an orthoferrite. Finally, for mixed materials, the first coordination sphere of a specific ion may not be completely correlated to the average measured by diffraction and the anisotropy axes may be poorly determined.

Doping induced strain has little effect on the (paramagnetic) ionic magnetic moment length, as the DFT calculations did not show any changes above the 1% level. However, for the various structures tried, the calculated ionic moments are reduced from the g = 2 limit such that μ_{Mn} = 3.6 μ_B (reduced from 4 μ_B for the free ion) and μ_{Fe} = 4.2 μ_B (reduced from 5 μ_B for the free ion).

At last, it is possible to try to understand the moment directions and magnitudes of AMFO. The usage of end-member parameters suggests better reproduction of experimental systems for lower dopings (x close to 0 or 1). Doping induced strain effects are qualitatively considered for higher dopings (x far from 0 or 1)

The model magnetic moments compare favorably to experimental data in the low-doped regime. There is a neutron diffraction study of the A-type and G-type magnetic moments in NdMn$_{0.8}$Fe$_{0.2}$O$_3$. [22] The saturation value of the A-type B-site moment is 2.69 μ_B from extrapolating the value above the onset polarization of Nd moments. These MC simulations found that $\langle S_{Mn}\rangle$[A-type] = 1.66 and $\langle S_{Fe}\rangle$[A-type] = 1.15 for NdMn$_{0.8}$Fe$_{0.2}$O$_3$. The calculated ionic moments then give an A-type long range order simulation value of 2.58 μ_B, with 2.39 μ_B from Mn and 0.19 μ_B from Fe. For the G-type B-site moment in NdMn$_{0.8}$Fe$_{0.2}$O$_3$, neutron diffraction results extrapolate to a saturation value of 0.6 μ_B. The simulations for NdMn$_{0.8}$Fe$_{0.2}$O$_3$ find $\langle S_{Mn}\rangle$[G-type] = 0.33 and $\langle S_{Fe}\rangle$[G-type] = 1.02, which give a net G-type moment of 0.65 μ_B, with 0.48 μ_B from Mn and 0.17 μ_B from Fe. The simulated spin collinearity for NdMn$_{0.8}$Fe$_{0.2}$O$_3$ of 0.91 (as opposed to 1 for an end-member) is another way to conceptualize the decreased ordered moment even as the local moments retain their magnitude. As for the direction, the experiment observes one irreducible representation, $\Gamma_5 = (G_S, A_M, F_L)$, which is consistent with D_{Mn} || Mn-O(l) || M dictating the anisotropy. The local short axis that is expected to set D_{Fe} is ambiguous as in NdMnO$_3$ Mn-O(s) || L, while in Nd$_2$MnFeO$_6$ Mn-O(s) || S and Fe-

O(s) || L. Regardless, it may be that the D_{Fe} axis is not parallel to the G-type axis as the iron spins are below the percolation limit and their order is subjugated to the manganese spins, where the Γ_5 order parameter only has non-zero G-type moments as G_S.

For the intermediate-doped regime, the model is not as well motivated and the comparison is less direct. Neutron diffraction has been reported for $NdMn_{0.5}Fe_{0.5}O_3$, [18,23] although the air firing of those samples is expected to introduce Mn^{4+} that is not included in this model. [14] Maximal G-type values of 2.42 μ_B [23] and 2.2 μ_B [18] are reported, both of which are less than the simple average of 0.5 × 4.2 μ_B Fe + 0.5 × 3.6 μ_B Mn = 3.9 μ_B Fe+Mn and greater than the Fe contribution alone. This incompleteness of the present model manifests in the incorrect model ordered G-type moments of 0.5 × 4.2 μ_B Fe + 0.5 × 3.2 μ_B Mn = 3.7 μ_B Fe+Mn and A-type moments of 0.5 × 0.07 μ_B Fe + 0.5 × 0.23 μ_B Mn = 0.15 μ_B Fe+Mn, suggesting strain induced anisotropy and short-rage order effects are important to correct these values. As for moment direction, in one report the G-type moment is found to rotate from $\Gamma_1 = (A_S, G_M, C_L)$ at higher temperatures to $\Gamma_3 = (F_S, C_M, G_L)$ at lower temperatures, [23] while the other makes no mention of moment direction at either 290 K or 4.3 K. [18] For both sets of diffractograms, the lowest temperature data show greater intensity on the 011 than the 101 (axes order as S, M, L) and the lowest angle data are then consistent with a linear combination of Γ_1 and Γ_5. At the highest temperatures, the observation of Γ_1 is consistent with manganese spins participating in the G-type order and dominating the anisotropy with $D_{Mn}||M \gg D_{Fe}$. The second magnetic transition beginning near T = 70 K [23] or T = 40 K [18] may be related to the second transition in the MC simulations. In the simulations, this transition is due to a parameter with $A_{\perp M}$, but no A-type order is reported for $NdMn_{0.5}Fe_{0.5}O_3$. Experimentally, magnetization and neutron depolarization show a FM component of ~0.1 μ_B evolving below the second transition, [23] and the high temperature Γ_1 has no FM component. This FM could be due to Mn^{4+} impurities causing double-exchange, weak FM from antisymmetric exchange as in NMO, strain induced $J_{MnMn}>0$, or a combination of all three. Irreducible B-site representations with both FM and G-type AFM are $\Gamma_3 = (F_S, C_M, G_L)$ and $\Gamma_5 = (G_S, A_M, F_L)$. One possibility to resolve this apparent inconsistency is that the second transition develops due to short range Mn-dominated-Γ_5-A_M order that is in direct competition with Γ_1-G_M order forcing a G-type rotation, and the weak-FM component due to manganese antisymmetric exchange could then have an F_L mode. Element specific magnetometry, quantification of Mn^{4+}, measurement of ion specific local structure, and measurement of chemical clustering for an $NdMn_{0.5}Fe_{0.5}O_3$ sample would be useful to understand this disagreement between the current model and experiment.

These calculations are expected to be relevant to Mn^{4+}-free $AMn_{1-x}Fe_xO_3$ (A = La, Pr, Nd, Sm), where the NN Heisenberg Hamiltonian works well. [24] A detailed experimental study of the LMFO phase diagram with minimal Mn^{4+} would be useful. The $PrMn_{1-x}Fe_xO_3$ (PMFO) phase diagram [63] shows iron spin-reorientations from x = 0.6 to 1, when sufficient manganese inclusion presents a Jahn-Teller distortion that quenches iron spin-reorientation. Similar to NMFO, PMFO shows a region of two magnetic transitions from x ≈ 0.35 to 0.5 that map well to

the phase diagram in Figure 6. The $SmMn_{1-x}Fe_xO_3$ is less studied, with a report of $SmMn_{0.25}Fe_{0.75}O_3$ [64] that is concerned mainly with the FeO_6 octahedral rotation induced spin-reorientations that are not considered here. Some insight may also be gained for specific regions of heavier rare-earths. The $TbMn_{1-x}Fe_xO_3$ series has a rich literature owing to the non-collinear magnetic order of the multiferroic $TbMnO_3$ end-member. [65] For low enough iron concentrations, the frustrating Mn NNN interactions can stabilize the $TbMnO_3$ spin-density-wave and cycloidal order, but doping interrupts that detailed balance for $x > 0.1$ and the A-type order from NN J_{MnMn} reappears. So, the doping region from $TbMn_{0.7}Fe_{0.3}O_3$ to $TbMn_{0.3}Fe_{0.7}O_3$ may be informed by this work as there are two B-site magnetic transitions with a similar doping effect as the $AMn_{1-x}Fe_xO_3$ (A = La, Pr, Nd, Sm) series. [66] Neutron diffraction is reported for the $x = 0.5$, $TbMn_{0.5}Fe_{0.5}O_3$ compound where a trade-off between $\Gamma_1 = (A_S, G_M, C_L)$ and $\Gamma_5 = (G_S, A_M, F_L)$ is seen as a function of temperature. [67] At 300 K, Γ_5 is modelled to be ~90%, gradually decreasing in fraction to a minimum of ~30% at T = 50 K, then increasing again to >90% at T = 10 K, at which point the Tb orders with an additional irreducible representation. Diffuse scattering attributed to Tb short range order is seen below T = 26 K. There are subtle changes of the lattice with temperature, but in all regions studied Fe-O(s) || D_{Fe} || S and the Mn-O(l) || D_{Mn} || M. At the highest temperature, it could be that D_{Fe}||S is increased due doping induced strain and sets the G-type direction, then there is a competition with D_{Mn}||M for the G-type direction, and then J_{MnMn}-influenced order may induce short-range-A-type that causes diffuse scattering and weak-FM.

VI. Conclusions

Features of $AMn_{1-x}Fe_xO_3$ (A = La, Nd; x = [0,1]) B-site magnetism are explained. Models for the anisotropy of octahedral S = 2, d^4 Mn^{3+} and S = 5/2, d^5 Fe^{3+} have been developed using ligand field theory that are connected to the geometry of the first coordination sphere, allowing strain effects on anisotropy to be investigated and show Mn anisotropy directions along the local long Mn-O bond and Fe anisotropy directions along the local short Fe-O bond. The strain effects on the superexchange that mimic possible environments of mixed Mn/Fe orthometallates have been calculated using density functional theory. Double perovskites have been simulated and yield ferromagnetic manganese to iron superexchange interactions and comparison of Monte Carlo simulations to experimental ordering temperatures of solid solutions further confirms the calculated J_{MnFe} parameters. Monte Carlo simulations compare quantitatively to experimental data for low dopings (e.g. $x \approx 0.2$) and provide qualitative insight into intermediate (e.g. $x \approx 0.5$) dopings. The experimentally observed non-monotonic interpolation of ordering temperatures when exchanging manganese with iron is reproduced here and is due to competition between symmetrically incompatible order parameters. While paramagnetic moments are not altered with doping, the ordered moment lengths in doping regions with phase competition are found to be less than their maximal values due to disordered non-collinearity of spins. Altogether, these results suggest that insight into interspecies interactions in systems can be found by considering a solid solution doping series. Such a study may be relevant to understanding interactions between

dissimilar transition metals with similar ionic radii that are difficult to stabilize as double perovskites.

Acknowledgements: Computing resources were made available through the VirtuES (Virtual Experiments in Spectroscopy) project, funded by Laboratory Directed Research and Development program (LDRD project No. 7739). Daniel Pajerowski is supported through the Scientific User Facilities Division of the Department of Energy (DOE) Office of Science, sponsored by the Basic Energy Science (BES) Program, DOE Office of Science.

Appendix A: Monte Carlo algorithm size effect

No rigorous comparison of performance against standard methods was made, but the onset of the phase transition for different values of L was checked. Three dimensional classical Heisenberg magnets on simple-cubic lattices have been studied extensively, and ratios of T_C/J between 1.4432 and 1.4446 for Monte Carlo and 1.4459 for series expansion are state-of-the-art. [61] Using periodic boundary conditions, $n_{update} = 200$ update loops per temperature, $n_\theta = 100$ angles for the discretization of θ', and $n_{burn} = 25$, three orders of magnitude for the number of sites were simulated for this code (L=10, L=22, and L=46). The derivative of energy with respect to temperature versus temperature and the mean of the size magnetization are two ways to visualize the phase transition, as shown in Figure 7. The scatter of data scales in the expected way with the number of sites averaging over space and time. Finite size effects of the periodic boundary condition tests tend to overestimate the phase transition, with fits to the magnetic order parameter giving $T_C(L=10) = 1.547\ JS^2$, $T_C(L=22) = 1.494\ JS^2$, and $T_C(L=46) = 1.458\ JS^2$. The L=22 size is a compromise between precision and convergence time, only overestimating the onset of order by 3 percent, and is used for simulations of AMFO that are presented in this work in comparison with experiment.

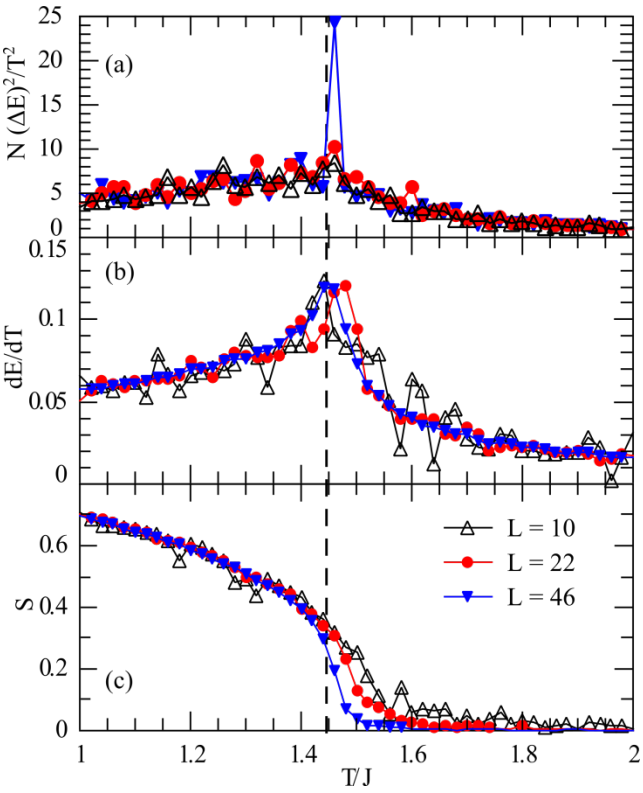

Figure 7: Monte Carlo algorithm calibration. There is a systematic reduction in ordering temperature and data scatter from (a) specific heat from fluctuations, (b) specific heat from energy derivative, and (c) magnetization when increasing the number of sites in this periodic boundary condition simulation. The dashed vertical line is the literature value of the transition temperature.

Appendix B: Angular overlap parameterization

The Mn^{3+} is a ^5D ground state $3d^4$ ion, which in O_h octahedral oxygen coordination has a ^5E_g ground state with S = 2. [68] From a cluster calculation with $r_{Mn\text{-}O}$ = 1.95 Å, [69] the energies of the first 5 excited states ($^3T_{1g}$, $^1T_{1g}$, ^1E, ^3E_g, $^5T_{2g}$) are 0.68 eV, 1.8 eV, 2.1 eV, 2.23 eV, and 2.4 eV. A best fit of the cluster calculation to the ligand field Hamiltonian without distortions and without spin-orbit coupling gives energies of 0.55 eV, 1.85 eV, 2.00 eV, 2.43 eV, and 2.25 eV, and there is a qualitative disagreement between the ligand field parametrization and the cluster calculation whereby the relative energies of ^5E_g and $^5T_{2g}$ have reversed order. The ratio of e_σ/e_π is 3.3, which is similar the value of 4 reported for the oxygen coordinated aqueous chromium ion. [38] The octahedral symmetry is lifted by Jahn-Teller distortion and from the distorted cluster calculation having $r_{Mn\text{-}O}$ = (1.90 Å, 1.95 Å, 2.14 Å), [69] the n parameter is extracted by fitting to the Jahn-Teller splitting, D_{JT} = 1.2 eV. The fit value of n = 5.74 is reasonable, as it lies

between the n = 5 scaling for crystal-field point charges and the n = 6 scaling for crystal field dipoles. [38] Finally, the full Hamiltonian is applied in comparison to the measured single-ion anisotropy constant, D_{Mn} = 0.16 meV, [42,70] to extract k. In this model, D_{Mn} is directly proportional to $\zeta^2 = \zeta_0^2 k^2$. The parameter set described here for Mn^{3+} is summarized in Table III.

The Fe^{3+} is a ^6S ground state $3d^5$ ion, which in octahedral oxygen coordination symmetry has a $^6A_{1g}$ ground state with S = 5/2. [68] This Fe^{3+} is not Jahn-Teller active and distortions from O_h symmetry are smaller than for the Mn^{3+} with a standard deviation in metal oxygen bond length of the order of 0.01 Å compared to ten times that for the Mn^{3+}. Taking the ratio of e_σ/e_π from the Mn^{3+}, the ligand field parameters can be directly extracted from the measured Δ_{OCT} = 1.69 eV ≡ $3e_\sigma - 4e_\pi$ from x-ray absorption. [71] The β_B, β_C, and n parameters are taken from the Mn^{3+} analysis. While anisotropy constants of LFO and NFO have been measured, the assumption used for Mn^{3+} that the dominant term is magnetocrystalline does not necessarily hold for orthoferrites as other anisotropy energies have the same order of magnitude and magnetic dipole interactions are one example. [72] In general, the value of k may be decreased due to electron delocalization from covalency and distortion away from O_h, and k > 0.9 for the hexaquo orbital singlet nickel, such that k =1 is reasonable for this compound. The zero field splitting is again directly proportional to $\zeta^2 = \zeta_0^2 k^2$. The parameter set described here for Fe^{3+} is summarized in Table III.

Table III. Ligand field parameters for Mn^{3+} and Fe^{3+} in pseudo-perovskite local environments of AMFO. The free ion values (B_0, C_0, and ζ_0) [38] are shown as a basis of comparison. The r_0 value is the value at which e_σ and e_π are as listed.

	Mn	Fe
B_0 / meV	118	128
B / meV	109	118
β_B	0.92	0.92
C_0 / meV	506	521
C / meV	472	484
β_C	0.93	0.93
e_σ / eV	1.25	0.94
e_π / eV	0.37	0.29
r_0	1.95	2.00
n	5.74	5.74
ζ_0 / meV	44	57
ζ / meV	23	57
k	0.54	1

The anisotropy of Mn^{3+} in LMO and NMO is an order of magnitude larger than the anisotropy of Fe^{3+} in LFO and NFO. The easy axis of Mn^{3+} is along the long bond of the oxygen octahedron

while the easy axis of Fe^{3+} is along the short bond of the oxygen octahedron when oxygen-metal-oxygen bonds are close to 90°.

References:

[1] S. Geller, J. Chem. Phys. **24**, 1236 (1956).

[2] A. P. Ramirez, J. Phys. Condens. Matter **9**, 8171 (1997).

[3] K. Yoshimatsu, K. Nogami, K. Watarai, K. Horiba, H. Kumigashira, O. Sakata, T. Oshima, and A. Ohtomo, Phys. Rev. B **91**, 054421 (2015).

[4] K. Ueda, H. Tabata, and T. Kawai, Phys. Rev. B **60**, R12561 (1999).

[5] L. Sun, Y.-W. Fang, J. He, Y. Zhang, R. Qi, Q. He, R. Huang, P. Xiang, X.-D. Tang, P. Yang, J. Chu, Y.-H. Chu, and C.-G. Duan, J. Mater. Chem. C **5**, 5494 (2017).

[6] Y. Du, Z. X. Cheng, S. X. Dou, X. L. Wang, H. Y. Zhao, and H. Kimura, Appl. Phys. Lett. **97**, 122502 (2010).

[7] T. Ahmed, A. Chen, D. A. Yarotski, S. A. Trugman, Q. Jia, and J. X. Zhu, APL Mater. **5**, 035601 (2017).

[8] T. Ahmed, A. Chen, B. McFarland, Q. Wang, H. Ohldag, R. Sandberg, Q. Jia, D. A. Yarotski, and J. X. Zhu, Appl. Phys. Lett. **108**, 242907 (2016).

[9] E. M. Choi, S. Patnaik, E. Weal, S. L. Sahonta, H. Wang, Z. Bi, J. Xiong, M. G. Blamire, Q. X. Jia, and J. L. MacManus-Driscoll, Appl. Phys. Lett. **98**, 012509 (2011).

[10] P. Liu, Z. X. Cheng, Y. Du, L. Y. Feng, H. Fang, X. L. Wang, S. X. Dou, P. Liu, Z. X. Cheng, Y. Du, L. Y. Feng, H. Fang, X. L. Wang, and S. X. Dou, J. Appl. Phys. **113**, 17D904 (2013).

[11] J. T. Zhang, X. M. Lu, J. Zhou, J. Su, K. L. Min, F. Z. Huang, and J. S. Zhu, Phys. Rev. B **82**, 224413 (2010).

[12] A. K. Kundu, R. Ranjith, B. Kundys, N. Nguyen, V. Caignaert, V. Pralong, W. Prellier, and B. Raveau, Appl. Phys. Lett. **93**, 052906 (2008).

[13] W. Tong, B. Zhang, S. Tan, and Y. Zhang, Phys. Rev. B **70**, 014422 (2004).

[14] Q. Huang, A. Santoro, J. W. Lynn, R. W. Erwin, J. A. Borchers, J. L. Peng, and R. L. Greene, Phys. Rev. B **55**, 14987 (1997).

[15] J. Lazurova, M. Mihalik, M. M. jr, M. Vavra, M. Zentkova, J. Briancin, M. Perovic, V. Kusigerski, O. Schneeweiss, P. Roupcova, K. V Kamenev, M. Misek, and Z. Jaglicic, J. Phys. Conf. Ser. **592**, 012117 (2015).

[16] J. Barrozo, Petrucio; Moreno, N. O.; Albino Aguiar, in *Adv. Mater. Res.*, edited by D. Z. de Florio, E. N. S. Muccillo, F. C. Fonseca, and R. Muccillo (2014), pp. 122–127.

[17] R. D. Shannon, Acta Crystallogr. Sect. A **32**, 751 (1976).

[18] I. O. Troyanchuk, M. V. Bushinsky, H. Szymczak, M. Baran, and K. Bärner, J. Magn.

Magn. Mater. **312**, 470 (2007).

[19] M. Mihalik, J. Lazúrová, M. Fitta, and M. Vavra, J. Magn. Magn. Mater. **345**, 125 (2013).

[20] W. C. Koehler and E. O. Wollan, J. Phys. Chem. Solids **2**, 100 (1957).

[21] H. Bruus and K. Flensberg, Oxford Grad. Texts 352 (2002).

[22] M. Mihalik, M. Mihalik, A. Hoser, D. M. Pajerowski, D. Kriegner, D. Legut, K. M. Lebecki, M. Vavra, M. Fitta, and M. W. Meisel, Phys. Rev. B **96**, 134430 (2017).

[23] A. Singh, A. Jain, A. Ray, P. B., R. Yadav, V. Nassif, S. Husain, S. M. Yusuf, T. Maitra, and V. K. Malik, Phys. Rev. B **96**, 144420 (2017).

[24] T. Kimura, S. Ishihara, H. Shintani, T. Arima, K. T. Takahashi, K. Ishizaka, and Y. Tokura, 3 (2002).

[25] Z. Yang, Z. Huang, L. Ye, and X. Xie, Phys. Rev. B **60**, 15674 (1999).

[26] T. Hashimoto, S. Ishibashi, and K. Terakura, Phys. Rev. B **82**, 045124 (2010).

[27] T. A. Mellan, F. Corà, R. Grau-Crespo, and S. Ismail-Beigi, Phys. Rev. B **92**, 085151 (2015).

[28] G. Kresse and J. Furthmüller, Comput. Mater. Sci. **6**, 15 (1996).

[29] G. Kresse and J. Furthmüller, Phys. Rev. B **54**, 11169 (1996).

[30] J. P. Perdew, K. Burke, and M. Ernzerhof, Phys. Rev. Lett. **77**, 3865 (1996).

[31] G. Kresse and D. Joubert, Phys. Rev. B **59**, 1758 (1999).

[32] P. E. Blöchl, Phys. Rev. B **50**, 17953 (1994).

[33] S. Van Der Walt, S. C. Colbert, and G. Varoquaux, Comput. Sci. Eng. **13**, 22 (2011).

[34] E. Anderson, Z. Bai, C. Bischof, L. S. Blackford, J. Demmel, J. Dongarra, J. Du Croz, A. Greenbaum, S. Hammarling, A. McKenney, and D. Sorensen, *LAPACK Users' Guide* (Society for Industrial and Applied Mathematics, Philadelphia, PA, 1999).

[35] J. J. Moré, D. C. Sorensen, K. E. Hillstrom, and B. S. Garbow, *The MINPACK Project, in Sources and Development of Mathematical Software* (Prentice-Hall, 1984).

[36] E. Jones, T. Oliphant, and P. Peterson, SciPy Open Source Sci. Tools Python (2001).

[37] H. Adamsky, T. Schonherr, and M. Atanasov, in *Compr. Coord. Chem. II*, edited by J. A. McCleverty and T. J. Meyer (Elsevier, Amsterdam, 2003), pp. 661–664.

[38] B. N. Figgis and M. A. Hitchman, *Ligand Field Theory and Its Applications* (Wiley-VCH, New York, 2000).

[39] E. Hovestreydt, M. Aroyo, S. Sattler, and H. Wondratschek, J. Appl. Crystallogr. **25**, 544

(1992).

[40] E. F. Bertaut, Acta Crystallogr. Sect. A **24**, 217 (1968).

[41] V. Skumryev, F. Ott, J. M. D. Coey, A. Anane, J.-P. Renard, L. Pinsard-Gaudart, and A. Revcolevschi, Eur. Phys. J. B **11**, 401 (1999).

[42] F. Moussa, M. Hennion, J. Rodriguez-Carvajal, H. Moudden, L. Pinsard, and A. Revcolevschi, Phys. Rev. B **54**, 15149 (1996).

[43] T. Chatterji, B. Ouladdiaf, and D. Bhattacharya, J. Phys. Condens. Matter **21**, 306001 (2009).

[44] R. J. McQueeney, J. Q. Yan, S. Chang, and J. Ma, Phys. Rev. B **78**, 184417 (2008).

[45] K. P. Belov, A. K. Zvezdin, A. M. Kadomtseva, and R. Z. Levitin, Sov. Phys. Usp. **19**, 574 (1976).

[46] T. Peterlin-Neumaier and E. Steichele, J. Magn. Magn. Mater. **59**, 351 (1986).

[47] C. A. L. Dixon, C. M. Kavanagh, K. S. Knight, W. Kockelmann, F. D. Morrison, and P. Lightfoot, J. Solid State Chem. **230**, 337 (2015).

[48] N. Koshizuka and K. Hayashi, J. Phys. Soc. Japan **57**, 4418 (1988).

[49] W. Sławiński, R. Przeniosło, I. Sosnowska, and E. Suard, J. Phys. Condens. Matter **17**, 4605 (2005).

[50] E. Constable, D. L. Cortie, J. Horvat, R. A. Lewis, Z. Cheng, G. Deng, S. Cao, S. Yuan, and G. Ma, Phys. Rev. B **90**, 054413 (2014).

[51] K. Park, H. Sim, J. C. Leiner, Y. Yoshida, J. Jeong, S. Yano, J. Gardner, P. Bourges, M. Klicpera, V. Sechovský, M. Boehm, and J.-G. Park, ArXiv:1705.09441v2 (n.d.).

[52] J. B. Goodenough, Phys. Rev. **100**, 564 (1955).

[53] J. Kanamori, J. Phys. Chem. Solids **10**, 87 (1959).

[54] See Supplemental Material at [URL will be inserted by publisher] for additional details of the DFT and LFT calculations.

[55] T. Saitoh, A. E. Bocquet, T. Mizokawa, H. Namatame, A. Fujimori, M. Abbate, Y. Takeda, and M. Takano, Phys. Rev. B **51**, 13942 (1995).

[56] T. Arima, Y. Tokura, and J. B. Torrance, Phys. Rev. B **48**, 17006 (1993).

[57] D. Treves, J. Appl. Phys. **36**, 1033 (1965).

[58] J. Rodriguez-Carvajal, M. Hennion, F. Moussa, A. H. Moudden, L. Pinsard, and A. Revcolevschi, Phys. Rev. B **57**, R3189 (1998).

[59] T. Mori, N. Kamegashira, K. Aoki, T. Shishido, and T. Fukuda, Mater. Lett. **54**, 238

(2002).

[60] R. Przeniosło, I. Sosnowska, P. Fischer, W. Marti, F. Bartolomé, J. Bartolomé, E. Palacios, and R. Sonntag, J. Magn. Magn. Mater. **160**, 370 (1996).

[61] P. Peczak, A. M. Ferrenberg, and D. P. Landau, Phys. Rev. B **43**, 6087 (1991).

[62] N. Das, P. Mondal, and D. Bhattacharya, Phys. Rev. B - Condens. Matter Mater. Phys. **74**, 1 (2006).

[63] M. Mihalik, Z. Jagličić, M. Fitta, V. Kavečanský, K. Csach, A. Budziak, J. Briančin, M. Zentková, and M. Mihalik, J. Alloys Compd. **687**, 652 (2016).

[64] J. Kang, Y. Yang, X. Qian, K. Xu, X. Cui, Y. Fang, V. Chandragiri, B. Kang, B. Chen, A. Stroppa, S. Cao, J. Zhang, and W. Ren, IUCrJ **4**, 598 (2017).

[65] M. Kenzelmann, A. B. Harris, S. Jonas, C. Broholm, J. Schefer, S. B. Kim, C. L. Zhang, S. W. Cheong, O. P. Vajk, and J. W. Lynn, Phys. Rev. Lett. **95**, 27 (2005).

[66] M. Mihalik, M. Mihalik, Z. Jagličić, R. Vilarinho, J. A. Moreira, E. Queiros, P. B. Tavares, A. Almeida, and M. Zentková, Phys. B Condens. Matter **506**, 163 (2017).

[67] H. S. Nair, T. Chatterji, C. M. N. Kumar, T. Hansen, H. Nhalil, S. Elizabeth, and A. M. Strydom, J. Appl. Phys. **119**, 053901 (2016).

[68] H. A. Jahn and E. Teller, Proc. Roy. Soc. **A161**, 220 (1937).

[69] L. Hozoi, A. H. de Vries, and R. Broer, Phys. Rev. B **64**, 165104 (2001).

[70] D. Talbayev, L. Mihaly, and J. Zhou, Phys. Rev. Lett. **91**, 17202 (2004).

[71] J. R. Hayes and A. P. Grosvenor, J. Phys. Condens. Matter **23**, 465502 (2011).

[72] R. Bidaux, J. E. Bouree, and J. Hammann, J. Phys. Chem. Solids **35**, 1645 (1974).